Digital Simulation of the Measured Electrochemical Response of Reversible Redox Couples at Microelectrode Arrays: Consequences Arising from Closely Spaced Ultramicroelectrodes

Allen J. Bard,*[1] Joseph A. Crayston,[2] Gregg P. Kittlesen,[2] Theresa Varco Shea,[1] and Mark S. Wrighton*[2]

Department of Chemistry, Massachusetts Institute of Technology, Cambridge, Massachusetts 02139, and Department of Chemistry, University of Texas, Austin, Texas 78712

Diffusion to arrays of closely spaced (1.2–0.2 μm) ultramicroelectrodes (50 μm × 2.3 μm) was studied by digital simulation and by examining the redox behavior of $Ru(NH_3)_6^{3+}$ in H_2O. Cylindrical diffusion of solution species resulted in quasi-steady-state currents at the microband electrodes. Generation–collection experiments, analogous to rotating ring–disk collection experiments, resulted in larger generator currents than those observed at a single microelectrode due to the back diffusion of products to the neighboring microelectrode. A collection efficiency of 93% was observed for the reoxidation of $Ru(NH_3)_6^{2+}$ generated at a central microelectrode 0.2 μm from two flanking collector microelectrodes. This experiment as well as generator–single collector electrode pairs was simulated at a two-dimensional rectangular expanding grid and yielded results in good agreement with the experiment. Predictions of the model that the collection efficiency principally depends on the gap size, rather than electrode width, were tested experimentally. The novel application of microelectrode arrays to the study of the follow-up reactions of electrogenerated intermediates is demonstrated.

The digital simulation of electrochemistry of ultramicroelectrode arrays is shown here to be successful in predicting the effect of variations in electrode geometry on the current response. Our results on the properties of arrays of closely spaced microelectrodes represent the most complete study where theory can be tested with experiment.

Already, *single* ultramicroelectrodes have attracted a great deal of interest for analytical applications (*1*). Apart from their obvious compactness, they exhibit: (1) enhanced diffusion to achieve steady-state or quasi-steady-state, diffusion-controlled currents; (2) low charging currents (*2*); and (3) reduced solution resistance effects (*3*). The enhanced diffusion has led to their use in studies of charge transfer kinetics (*4*, *5*).

Recently it has been shown that it is possible to fabricate *arrays* of more than one ultramicroelectrode, each of which is individually addressable (*6–10*). Such arrays consist of microband electrodes, ca. 50 μm long and 2-3 μm wide, with an interelectrode spacing of the order of one to several micrometers (*6–13*). The photolithographic techniques used in the manufacturing process permit a very small spacing (1.2 μm) between electrodes. This makes them suited for use as charge flow control devices based on molecular materials (6–8, *11–13*), in which charge transport is usually very slow. Such devices may find applications as chemical sensors with built-in signal amplification (*14*). Previously described devices includes those that mimic transistor (*6–8*) and diode (*11*, *12*) characteristics with a spacing of 1.2 μm. Recently, a transistor-like device consisting of a poly(3-methylthiophene) film covering two microelectrodes has been exploited as a sensor for H_2 and O_2 (*13*).

The close electrode spacing (1.2 μm) has a profound effect on the solution amperometric response, as will be fully described in the Experimental Section of this paper (part II). Essentially, each microelectrode displays a sigmoidal current response in linear potential sweep voltammetry. This type of response arises from the enhanced mass transport due to nonlinear diffusion (*1–3*). Radial diffusion to the edges of microelectrodes contributes significantly to the overall diffusion and results in quasi-steady-state currents for moderate sweep rates with reversible redox couples. This diffusional flux affects various properties, but the most striking effect of an array of closely spaced electrodes where the diffusion layers overlap is that it becomes possible to detect the electrogenerated products at the adjacent electrodes. For example, the reduced form of a solution species generated at one microelectrode may be "collected" at adjacent microelectrodes, which are held at a potential where oxidation can occur (as indicated by an anodic current). The situation is analogous to collection experiments using conventional rotating ring–disk electrodes (RRDE) of macroscopic dimension (*15*, *16*). Thus, one can define a *collection efficiency* representing the ratio of currents at the generator and collector electrodes. However, as opposed to RRDE experiments, where the current at the disk is unaffected by the ring, for closely spaced stationary electrodes products at the collector can diffuse back to the generator electrode and be electrolyzed there. Thus, an additional *feedback current* at the generator can be observed. Finally, the current at one electrode can affect that at its neighbor when both are at the same potential, because the diffusion layers overlap. This is analogous to *shielding* at the RRDE. For a deeper understanding of the effects of electrode width and interelectrode gap spacing on the collection efficiency, feedback, and shielding, we used digital simulation techniques to model the microelectrode arrays. As described in part I, this model predicts a collection efficiency that is in agreement with experiment.

Finally, we show how it is possible to apply such a digital simulation in the future to a more complex situation, namely, a catalytic follow-up (or EC′) reaction (*17*) represented by eq 1 and 2. Catalytic currents have already been observed at

$$A^{m+} + ne \rightleftarrows A^{(m-n)+} \quad (1)$$

$$A^{(m-n)+} + B \rightarrow A^{m+} + B^{n-} \quad (2)$$

a *single* ultramicroelectrode (*18*, *19*), but not at an array of several electrodes, each of which may be individually potentiostated so that, in principle at least, all of the species in reactions 1 and 2 may be determined separately, provided that their electrode potentials are sufficiently different. Thus, the array of ultramicroelectrodes could function not merely as a

[1] University of Texas.
[2] Massachusetts Institute of Technology.

0003-2700/86/0358-2321$01.50/0

rotating ring–disk electrode but also as a split ring–disk electrode (*20*), capable of detecting up to seven intermediates.

EXPERIMENTAL SECTION

Ultramicroelectrode Arrays. In the arrays of eight Au microelectrodes, each was 50 μm long, 2.3 μm wide, 0.1 μm thick, and spaced 1.3 μm apart. Complete details of the fabrication of arrays on p-Si/SiO_2/Si_3N_4 substrates are given in earlier reports (*6–8, 11–13*). The arrays of two Au microelectrodes were designed with the aim of reducing the width and spacing dimensions for the particular application of decreasing the amount of polymer necessary to make the type of diode described in previous work (*11, 12*). The fabricated microelectrodes were 50 μm long, 1.2 μm wide, 0.1 μm thick, and interspaced by 0.9 μm. These geometries approach the practical limits imposed by the GCA Mann 4800 Wafer Stepper and positive photoresist. The M.I.T. Microelectronics Laboratory Wafer Stepper has successfully patterned 0.6 μm lines and spaces in MacDermid Ultramac PR-914 positive photoresist.

Prior to use, the electrode surfaces were cleaned by an rf O_2 plasma etch to remove residual photoresist, followed by cycling the potential at each electrode between −1.6 V and −2.0 V vs. SCE in 0.1 M aqueous K_2HPO_4, ca. 5 cycles at 200 mV/s to evolve H_2. Other conventional and more stringent chemical and electrochemical cleaning led to electrode damage. Pt was deposited on each electrode from 2 mM K_2PtCl_4 in 0.1 M aqueous K_2HPO_4. At each electrode, 0.2 μC was passed. The resulting platinized electrodes of an eight-wire array were 2.5 μm wide and interspersed by 1.0 μm. The dimensions were determined by scanning electron microscopy using a Cambridge Mark 2A Stereoscan with a resolution of 20 nm, after first coating the array with ca. 200 Å of Au to minimize problems from surface charging. The platinized electrodes of a two-wire array were 1.5 μm wide and interspaced by 0.8 μm. The interelectrode spacing was significantly reduced by depositing more Pt from solution. Upon passing a total charge of 2.5 μC at each of two adjacent electrodes of an eight-wire array, the electrodes were 3.1 μm wide and separated by 0.3 μm. Another strategy was to platinize the electrode lightly by passing 0.2 μC, and then to platinize the neighboring electrode more heavily by passing 4.0 μC. The heavily platinized electrode was 4.1 μm wide and separated from the lightly platinized one by 0.3 μm. Two-wire arrays were similarly lightly/heavily platinized by passing 0.2 μC and 1.75–2.0 μC, respectively.

Platinization of the Au electrodes was desirable in the Ru^{3+} generation–collection experiments for reasons of: (1) greater lifetime of the quasi-steady-state current for Ru^{3+} reduction—presumably adsorption of impurities with time led to a decreased current and a "flattening" of the sigmoidal i–V curve, and (2) providing a means of reducing the interelectrode spacing. However, the quinone experiments were conducted at the unplatinized Au electrodes so that there was less interference from direct O_2 reduction at the electrode. The Au electrodes were cleaned (as described above) prior to each measurement to obtain reproducible currents.

Gold electrodes were deliberately removed by electrochemically cycling between 0.0 V and +1.8 V vs. SCE in 0.1 M KCl solution until the current at 1.8 V decayed to zero. Alternatively, the electrode was potentiostated at +1.8 V vs. SCE. This removed both the ca. 0.1 μm thick Au electrode and the ca. 60 Å layer of Cr, so that zero current was observed in response to 5 mM $Ru(NH_3)_6Cl_3$. This lift off procedure was also attempted in a 0.1 M NaCN solution and cycling between 0.0 V and +0.5 V. However, preliminary optical microscopic and electrochemical examination suggested that the Au layer was removed, but the Cr layer was not affected.

Chemicals. Triply distilled H_2O (EM Science) was used for all solutions with various supporting electrolytes: KCl, LiCl, $LiClO_4$, and $LiNO_3$ were used as received. $Ru(NH_3)_6Cl_3$ (Strem) was also used as received. 2,5-Dichloro-3,6-bis[[2-(dimethylpropylamino)ethyl]amino]benzoquinone was prepared (*21*) by similar methods to those previously published for naphthoquinone derivatives (*22, 23*).

Electrochemical Equipment. Electrochemical plating of Pt onto the Au microelectrodes was accomplished with a Princeton Applied Research Model 173 potentiostat/galvanostat, Model 179 digital coulometer, and Model 175 Universal Programmer. The remaining electrochemical experiments were performed with a Pine Model RDE4 bipotentiostat and recorded on a Kipp and Zonen BD91 XYY't recorder. All potentials were controlled relative to an aqueous saturated calomel electrode (SCE). Electrochemical measurements were carried under N_2 or Ar at 22 °C, unless otherwise stated.

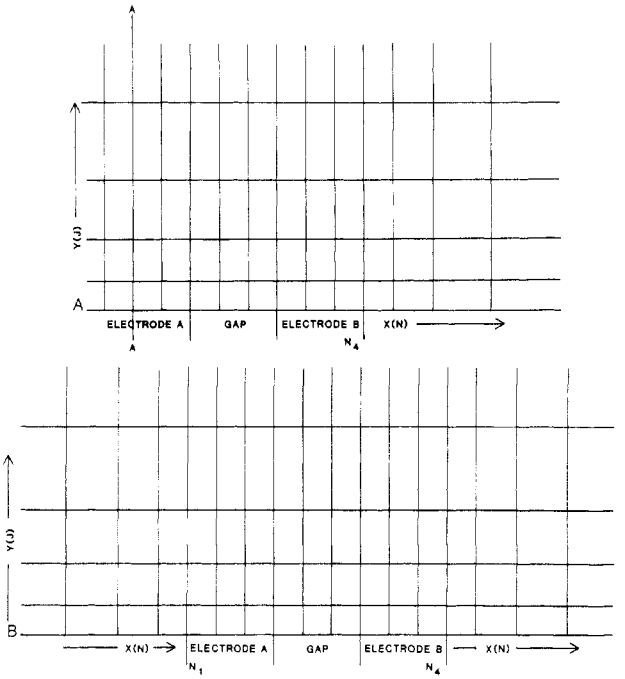

Figure 1. (A) Two-dimensional space grid used for the simulation of the three microelectrode array. The grid begins expanding after element N4, the last uniform element in the *N* direction. The grid expands also from the substrate in the *J* direction. The axis of symmetry through electrode A permits the simulation of half of the array. (B) Space grid used for the simulation of two-electrode pairs. To the right of N4 and in the *J* direction, the grid is the same as A. However, to the left of N1, the grid also expands exponentially.

Digital Simulations. All computations were carried out on the UT-CDC 6000 dual cyber computer (Control Data Corp.)

PART I. SIMULATION OF PATTERNED ARRAY ELECTRODES FOR ELECTROCHEMISTRY

Model and Tests of the Model. Digital simulation of a single microband electrode and arrays of electrodes generally followed previous practice (*24, 25*). To simulate the ultramicroelectrode array, a two-dimensional space grid was set up, Figure 1A, where the two electrodes A and B, the generator and collector, were separated by a gap. Because of the small height to width ratio, 1 to 23, of the experimental arrays, the top of the electrode was assumed to lie in the plane of the substrate, i.e., the height of the electrode in the *J* direction was taken to be zero. The width of the electrodes in the *N* direction, as well as the gap width, was varied by varying the number of boxes corresponding to the electrodes and the interelectrode spacing. In addition, the axis of symmetry through electrode A permitted the simulation of half of the three-electrode array as well as the single band electrode and reduced the amount of computer time and storage space needed. Figure 1B shows the grid configuration adopted for the simulation of generator–single collector pairs.

To further conserve computation time and extend the simulated times to correspond to the rather long experimental times required to attain quasi-steady-state behavior, an exponentially expanding space grid (*26–28*) was added in the *J* direction, perpendicular to the electrode surface, parallel to the substrate (Figure 1). However, the solution boxes above the electrodes and gap in the *N* direction were represented by a uniform space grid and were treated in the usual way (*24, 25*). Details of the mathematical treatment of the digital

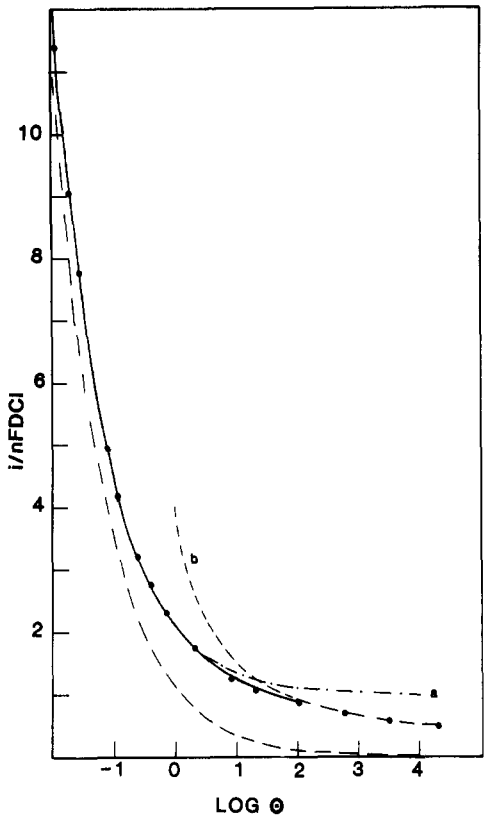

Figure 2. Normalized current, $i/nFDCl$ vs. log ($4Dt/W^2$). The solid line is the theoretical curve calculated in ref 29. The dashed curve (- - -) is the theoretical Cottrell behavior. Curve a was calculated by eq A17 and curve b by eq A16. The circles are simulated results.

simulation are given in the Appendix.

The validity of the model was demonstrated by applying the simulation to a single band electrode. In the test case, we consider a potential step to electrode A while electrode B was missing, i.e., the grid begins expanding at the edge of electrode A in the N direction and the solution contained only species Ox. We assumed total mass-transport-controlled conditions, with the concentration of Ox at the electrode surface going instantaneously to zero and the mass transport solely by diffusion. A typical simulated current–time (i–t) response compared to the numerical solution for a potential step at a microband electrode recently reported by Tallman et al. (*29*) is shown in Figure 2. The i–t response can be described in terms of three time domains that are dependent upon the magnitude of the dimensionless parameter $\theta = 4Dt/W^2$ (eq A15) where D is the diffusion coefficient, t is the time, and W is the electrode width. At very short times, $\theta < 3 \times 10^{-5}$ (corresponding to ca. 65 ns when $W \sim 1$ μm), the flux to the electrode surface is approximated by semiinfinite linear diffusion and the current decays as a function of $t^{-1/2}$ (Cottrell conditions) shown by the dashed line in Figure 2. This time regime was not observed in the digital simulation where the earliest simulation times correspond to real times of the order of microseconds.

In the limit of long times, $\theta <$ ca. 30, the current approaches that expected for a hemicylinder and decays as $(\ln t)^{-1}$ (Figure 2, curve b) (*29*). For the time domain of $0.01 \leq \theta \leq 1$, the current can be approximated by eq A17 (Figure 2, curve a) (*29*). Over the range of θ from 0.01 to 10000 simulated currents agreed with Coen, Cope, and Tallman's (*29*) numerical solution for a microband electrode within 3%, demonstrating the validity of the simulation model for a microband electrode over 6 orders of magnitude of θ thus providing confidence that the digital simulation could be applied to microelectrode arrays and determination of collection efficiencies, feedback, and shielding effects.

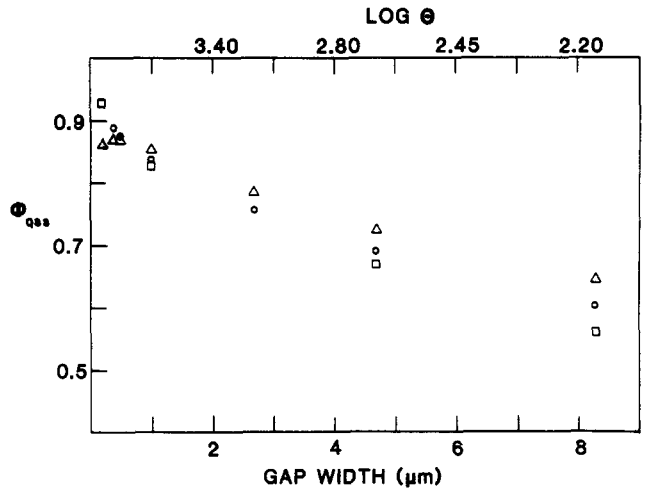

Figure 3. Collection efficiency, ϕ_{ss}, as a function of the interelectrode gap for a single generator, and a pair of flanking collector electrodes ($W_G = W_C = 1$ μm). Squares are experimental points (part II). The circles are simulation results at the same value of log $\theta_{GAP} = 4$ as the experimental points. Triangles are theoretical values calculated by eq 4.

Note that the microband electrode (in common with the cylindrical or hemicylindrical electrode) does not attain a true steady-state current; spherical and embedded disk electrodes do. However, at sufficiently long θ values ($\theta \geq 100$), the rate of decay of current is small; we call this the "quasi-steady-state" region. Feedback from the collector electrode tends to decrease even more the rate of decay, and the onset of natural convection can produce steady-state currents. For electrodes with W = ca. 1 μm, the quasi-steady-state region is attained after about 0.1 s. The quoted quasi-steady-state efficiencies here correspond to log $\theta \sim 3.3$, or experimental times of the order of t ca. 3.5 s. In this region the normalized currents change less than 5% for a 10-fold change in θ.

Simulation of an Array and Dependence of Collection Efficiency on Electrode Geometry. Half of the array is shown in Figure 1A, and results that apply to a central generator electrode and a pair of flanking collector electrodes will be discussed first. Because of the large width at height ratio, 23 to 1, the electrodes were considered to be in the plane of the substrate, so the height in the J direction was zero. At electrode A the reduction reaction Ox + e^- → Red occurs, as described in the previous section. However, now a potential is applied to electrode B such that the Red produced at electrode A is reoxidized, Red → Ox + e^-. This type of experiment is similar to that at a rotating ring–disk electrode (*15*, *16*) with the exception that now diffusion, not convection, is the primary means of mass transport. The geometric considerations necessary to maximize the amount of Red reaching electrode B will be discussed in the remainder of this paper.

To determine the effect of changing a geometric parameter, such as the gap or electrode width, the collection efficiency was studied. The collection efficiency, ϕ_{ss}, is the ratio of the quasi-steady-state current for Ox produced at the collector electrode, B, divided by the current for reduction of Ox at the generator electrode, A; see eq 3.

$$\phi_{ss} = (Z_B/Z_A)_{ss} \quad (3)$$

Simulated collection efficiencies for a generator and a pair of flanking collector electrodes of equal width (W_G and W_C = 1–4 μm) are shown by the circles in Figure 3. These are plotted in terms of the convenient dimensionless parameter $\theta_{GAP} = 4Dt/W_{GAP}^2$, where W_{GAP} is the gap width. The simulated points could be fit by the empirical equation

$$\phi_{ss} = 0.095 + 0.33 \log \theta_{GAP} - 0.035(\log \theta_{GAP})^2 \quad (4)$$

Table I Comparison of Collection Efficiencies for Various Electrode Sizes

electrode width,[a] μm	ϕ[b]
1.0	0.85
1.7	0.87
2.0	0.87
3.3	0.88

[a] For $W_G = W_C$; $W_{GAP} = 1$ μm. [b] ϕ calculated at log $\theta_{GAP} = 4.3$ corresponding to $D = 7.1 \times 10^{-6}$ cm²/s, $t = 7$ s.

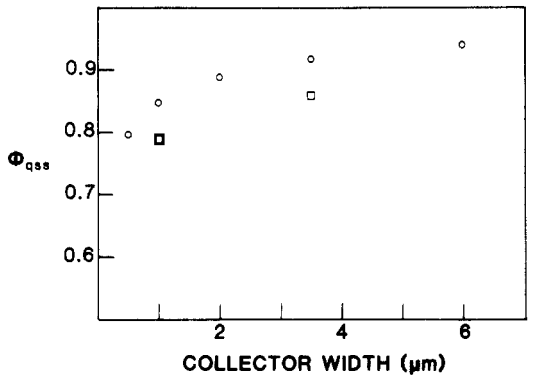

Figure 4. Collection efficiency, ϕ_{ss}, vs. the collector electrode width. The simulated collector widths were varied from 0.5 to 6 μm (circles) while the experimental widths were varied from 1 to 3.5 μm (squares) for the single generator, double collector electrode configuration. $W_G = 1$ μm, $W_{GAP} = 1$ μm, log $\theta_{GAP} = 4$.

The experimental results shown in Figure 3 will be discussed in part II. The results in Figure 3 and eq 4 indicate that, as intuitively expected, the collection efficiency is maximized as the gap width is decreased.

Another consideration in the construction of interdigitized ultramicroelectrode arrays concerns the width of the generator (W_G) and collector (W_C) electrodes, since the quasi-steady-state current (eq A16 and A17) is a function of the width. To maximize the current, a large width is desirable. However, a large width provides a greater lateral surface area from which the species Red can escape into the bulk. Therefore, a compromise between larger, more easily measured currents and minimizing loss due to diffusion out into the bulk must be made. However, for the electrode widths shown in Table I, where $W_G = W_C$ was varied from 1 to 3.3 μm with a 1-μm gap width, the collection efficiency ϕ_{ss} is the same within the error of the simulation (3%). While there is no discernible difference in ϕ_{ss} when the ratio of generator and collector is unity, when the ratio is not unity, the collection efficiency is found to depend on the collector electrode width. In Figure 4, ϕ_{ss} is plotted as a function of collector width for a generator electrode with two flanking collector electrodes, where the generator electrode width, the interelectrode gap, and θ are held constant. The squares are experimental points, discussed in part II. As expected, the collection efficiency increased as the collector electrode width increased from 0.5 to 6 μm with $W_G = 1$ μm and $W_{GAP} = 1$ μm. The increase in ϕ_{ss} is largest for $W_C \sim W_G$ and becomes less important for $W_C \geq 4$ μm. Thus, both the gap size and the ratio of the collector and generator electrode widths must be considered in the design of microelectrode arrays. One gains efficiency by minimizing the gap width while the ratio of the collector to generator widths should be greater than unity to maximize collection.

The digital simulation model could also be used to model a pair of microband electrodes (generator and single collector) of interest in experiments described in part II. The simulation grid used is shown in Figure 1B and the mathematical details are discussed in the Appendix. Simulated results of the collection efficiency, ϕ_{ss}, as a function of the interelectrode

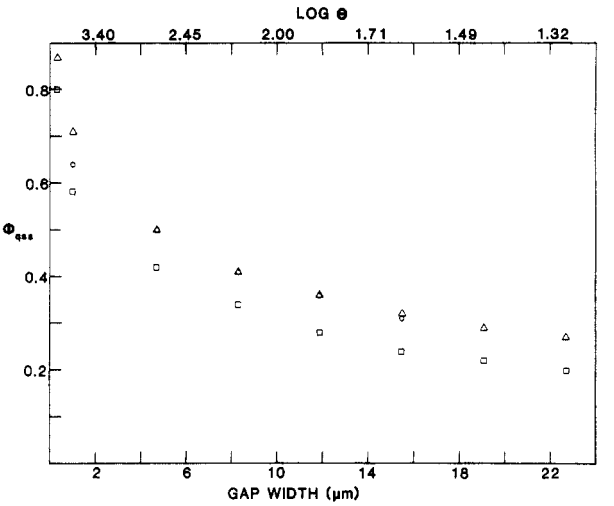

Figure 5. Collection efficiency, ϕ_{ss}, as a function of gap width for the generator–single collector pair. Simulated results (circles) correspond to gap widths of 1 to 15.5 μm while experimental results (squares) are for gaps of 0.5–22.7 μm. Theoretical results (triangles) were calculated by eq 5 for $D = 7.1 \times 10^{-6}$ cm²/s, $t = 3.5$ s, $W_G = 1$ μm.

gap width, W_{GAP}, are given in Figure 5. The collection efficiency can be approximated by eq 5 (with a coefficient of correlation of 0.997). Equation 5 is useful for estimation of

$$\phi_{ss} = 0.033 + 0.21 \log \theta_{GAP} - 0.016(\log \theta_{GAP})^2 \quad (5)$$

the observed experimental collection efficiencies for gaps of 0.5–23 μm. As expected, the ϕ_{ss} values for a pair of electrodes are smaller than those for flanking collectors (compare Figures 3 and 5).

Effect of Shielding and Feedback. When the array of ultramicroelectrodes was operated in the generator–collector electrode mode, the current response mimicked the steady-state behavior observed at the RRDE as previously demonstrated. As noted, the primary means of mass transport was by diffusion, which is responsible for the closely related shielding and feedback effects.

For the RRDE, the shielding experiment involves reducing the amount of Ox that reaches the ring, where the ring reaction is $Ox + e^- \rightarrow Red$, by applying a potential to the disk (e.g., $E_D = E_R$) to cause the same reduction reaction to occur. In the corresponding experiment with the array, the adjacent electrodes were held at the same potential, $E_G = E_C$, where E_G and E_C are the potentials of the generator and collector electrodes, respectively. As the electrolysis proceeds, the diffusion layers overlap, shielding each electrode. This shielding effect reduced the quasi-steady-state current at three electrodes in the array when compared to the sum of the currents expected at three independent electrodes. We define this reduction in current as the *shielding factor*, S_F, given by eq 6 for equal sized electrodes, where Z_i is the current at each

$$S_F = 1 - \frac{\sum_{i=1}^{q} Z_i}{qZ} \quad (6)$$

of the q electrodes in the array and Z is the current observed for a single electrode, with all other electrodes at open circuit. The shielding factor is a measure of the degree of overlap of the diffusion layers and approaches zero in the absence of shielding (e.g., for electrodes widely spaced apart). The simulation results for the quasi-steady-state currents at three electrode arrays are given in Table II. The shielding effect is more pronounced on the inner (generator) electrode than on the flanking (collector) electrodes, because the inner electrode is blocked from nonlinear diffusion paths from both sides while the outer electrodes are only blocked from one side.

Table II. Simulation of Effects of Feedback and Shielding[a]

gap width, μm	electrode width, μm: generator	electrode width, μm: collector	normalized currents: with feedback Z_G	with feedback Z_C	with feedback ϕ_{ss}	without feedback $Z_{G,0}$	without feedback Z_C	without feedback ϕ_{ss}	shielding Z_G	shielding Z_C	shielding Z_{tot}	shielding factor	feedback factor
1.0	1.0	0.5	1.09	0.87	0.80	0.50	0.40	0.80	0.22	0.42	0.64	0.56	0.54
1.0	1.0	1.0	1.14	0.97	0.85	0.50	0.43	0.85	0.18	0.50	0.68	0.57	0.56
1.0	1.0	6.0	1.20	1.13	0.94	0.50	0.47	0.94	0.07	0.83	0.90	0.57	0.58
2.7	1.0	1.0	0.88	0.67	0.77	0.50	0.39	0.77					0.43
0.5	1.0	1.0	1.37	1.21	0.88	0.50	0.44	0.88					0.64

[a] Z_G and Z_c are normalized generator and collector electrode currents, respectively, ϕ_{ss} is the quasi-steady-state collection efficiency (eq 3); the shielding and feedback factors are defined in eq 6 and 7, respectively. For a single generator and two flanking collector electrodes.

A phenomenon related to shielding but not possible at the RRDE is feedback. When the reduced species reaches the collector electrode, it is reoxidized to Ox that can diffuse back to the generator electrode. Thus, the collector electrodes act as a source and increase the flux of Ox to the generator. The effect of feedback was observed in the increased magnitude of the quasi-steady-state generator currents (see Table II). In generator–collector experiments where the reactions were all reversible, the generator currents were increased by the feedback factor, F_B, given in eq 7, where $Z_{G,0}$ is the steady-state

$$F_B = 1 - (Z_{G,0}/Z_{G,C}) \quad (7)$$

current without feedback and $Z_{G,C}$ is the steady state generator current with feedback. Typical effects of feedback with three electrode arrays are given in Table II. It should be noted that at the same log $\theta = 4.3$, the collection efficiencies are the same with and without feedback, although the magnitudes of the generator and collector currents are smaller without feedback.

In summary, the predictions of the digital simulation are as follows: (1) the collection efficiency is strongly dependent on gap size and to a lesser extent on the collector electrode width; (2) by use of eq 4 for a three-electrode array or eq 5 for a two-electrode pair, the collection efficiency can be calculated for a known diffusion constant, time, and interelectrode gap (i.e., θ_{GAP}); (3) shielding and feedback are shown to be important at electrodes of these dimensions; (4) agreement between the simulation predictions and experiment are within 10% and agreement between the simulation and theory is better than 3% for a single microelectrode.

PART II. EXPERIMENTAL RESULTS AND DISCUSSION

Electrochemical Characterization of Microelectrode Arrays. Each Au electrode of an array was individually addressable. Generally, a small amount of Pt (0.2 μC corresponding to a coverage of 0.86 μmol/cm²) was electrochemically deposited onto each microelectrode to yield a consistently fresh electroactive surface prior to electrochemical experimentation. Figure 6 shows linear potential sweep cyclic voltammograms for the reduction of $Ru(NH_3)_6^{3+}$ at each microelectrode of an eight-electrode array. The solution was not stirred during the measurement. That there was no cathodic current peak is a consequence of the narrow width of the microelectrode. At a larger electrode at the same sweep rate, a cathodic current peak would be observed due to the depletion of $Ru(NH_3)_6^{3+}$ near the electrode surface. On the return scan an anodic current peak would also be observed due to the oxidation of $Ru(NH_3)_6^{2+}$ generated in the negative sweep. At the microelectrode radial diffusion to the edges of the microelectrode was significant and combined with diffusion normal to the microelectrode surface to deliver the redox species to the microelectrode at a rate approximately equal to the electrolysis rate. Hence, a steady-state current was observed at slow sweep rates and low redox reagent concentrations. As shown in part I, it was not necessary for non-

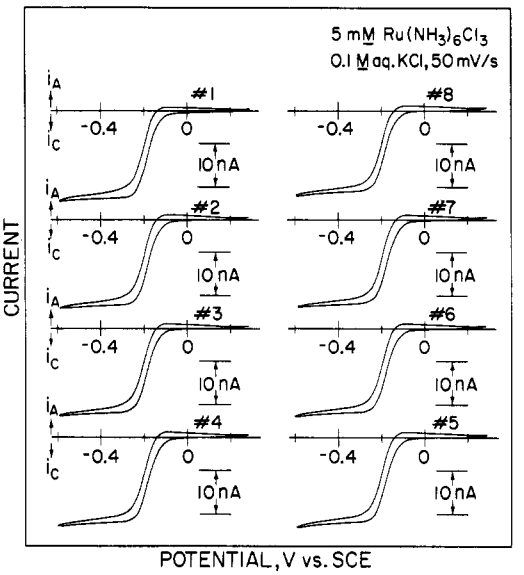

Figure 6. Cyclic voltammetry, 50 mV/s, of an array of eight microelectrodes in a 0.1 mM LiCl solution containing 5 mM $Ru(NH_3)_6^{3+}$.

diffusional hydrodynamic flow to be invoked. The quasi-steady-state cathodic currents in Figure 6 are all nearly identical, demonstrating the success of the encapsulation and Pt deposition techniques used in the array fabrication. The magnitude of the current can be calculated from eq 8 (*29*) for the mass transport limited current at a microband electrode,

$$i = nFDCl[5.553/(\ln \theta) - 6.791/(\ln \theta)^2],\ \theta = 4Dt/W^2 \quad (8)$$

where l is the length of the electrode, W is the width of the electrode, and t is the characteristic time. Typically θ was about 215 for our electrodes, so that for the experiment in Figure 6, eq 8 predicts a current of 13.7 nA compared to ca. 19 nA observed. At a θ of 215, the simulation and theory are in very good agreement. The normalized current function, Z (see eq A16), for the experiment in Figure 6 is 1.11 compared with 0.80 calculated by eq 8 and 0.78 calculated by the simulation.

The results of a generation–collection experiment analogous to a rotating ring–disk electrode collection experiment are given in Figure 7. The potentials of two adjacent microelectrodes were independently controlled by a bipotentiostat. Again, forced convection was not necessary in order to observe quasi-steady-state currents. In the experiment summarized by Figure 7, the potential of one electrode, the generator electrode, was swept in a negative direction linearly in time through the formal potential of $Ru(NH_3)_6^{3+/2+}$. Simultaneously, the potential of the adjacent electrode, the collector electrode, was held fixed at a value such that the $Ru(NH_3)_6^{2+}$ generated was oxidized to $Ru(NH_3)_6^{3+}$. A larger steady-state current (42% greater) was observed at the generator electrode

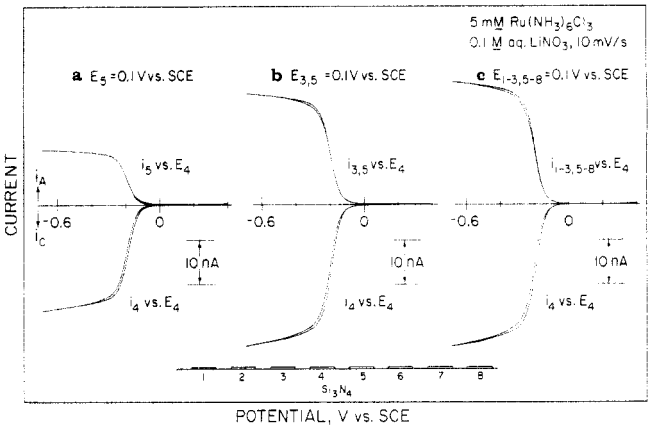

Figure 7. Generation/collection experiment in 5 mM $Ru(NH_3)_6Cl_3$ in 0.1 M aqueous $LiNO_3$ as a function of the number of collector electrodes. Microelectrode no. 4 was the generator electrode in each case. The potential of the generator electrode was swept between +0.4 and −0.7 V vs. SCE at 10 mV/s while the potential of the collector electrodes was held at +0.1 V vs. SCE. Collector electrodes: (a) single adjacent electrode no. 5; (b) microelectrodes no. 3 and no. 5; (c) electrodes no. 1–3 and no. 5–8.

Table III. Distance Dependence of Observed Collection Efficiency Using One Generator Electrode and Two Symmetrically Disposed Collector Electrodes[a]

generator electrode current, nA		collector electrode current, nA		separation,[b] μm	collection efficiency, %
no. 4	36.8	no. 3, 5	30.4	1.0	83
no. 4	25.6	no. 2, 6	17.2	4.7	67
no. 4	22.8	no. 1, 7	12.8	8.3	56

[a] Mean values determined from several different lightly platinized microelectrode arrays. Errors: separation (SEM photographs), ±0.1 μm; collection efficiencies, ±3%. [b] Separation between generator and collector nearest edges.

than when no collector electrode was used. This is the manifestation of feedback associated with closely spaced electrodes discussed in part I. The point is that the collector electrode was an additional source of $Ru(NH_3)_6^{3+}$ to the generator electrode. A total of 51% of the generated $Ru(NH_3)_6^{2+}$ was collected at one adjacent microelectrode, Figure 7. Collection efficiencies were typically 51–60% between adjacent lightly platinized microelectrodes with a 1.0-μm separation between nearest edges. The significant finding is that more than 50% of the generated $Ru(NH_3)_6^{2+}$ can be collected on only one side of the generator electrode. The collection efficiency was the same when the electrode on the other side of the generator was used as a collector. In other words, there is a symmetry of the system in the sense that any pair of adjacent electrodes in a generation–collection experiment will give rise to the same collection efficiency.

Now we examine the first situation investigated in the digital simulation. For two collector electrodes, one on either side of a centrally positioned generator electrode, the collection efficiency was dramatically increased to 79%, Figure 7b. Here, the limiting current observed at the generator electrode was 88% greater than when no collector electrodes were used, F_B = 0.47, demonstrating significant consequence from feedback. Simulation results predict F_B = 0.44 for this electrode geometry at log θ = 3.1. By connecting seven microelectrodes as collector electrodes the collection efficiency only increased to 86%, Figure 7c. Clearly, inclusion of those electrodes lying farther away from the central generator electrode did little to increase the collection efficiency beyond 79%. This result is consistent with part I as shown in Figure 4.

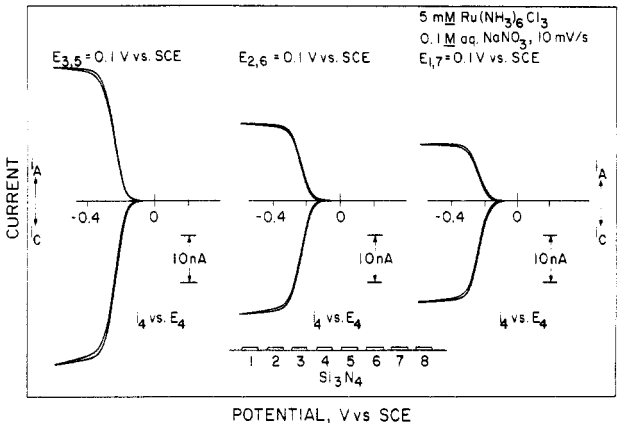

Figure 8. Generation/collection experiment in 5 mM $Ru(NH_3)_6Cl_3$ in 0.1 M aqueous $NaNO_3$ using a central generator microelectrode no. 4 and symmetrical pairs of collector electrodes. (L–R: no. 3, 5; no. 2, 6; no. 1, 7).

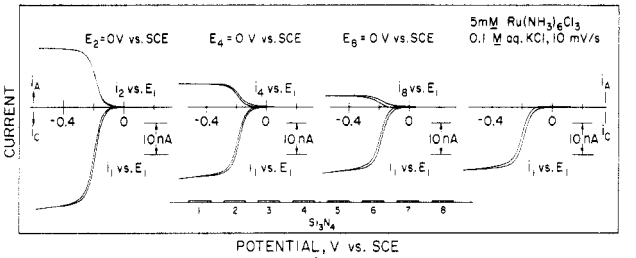

Figure 9. Generation/collection experiment in 5 mM $Ru(NH_3)_6Cl_3$ in 0.1 M aqueous KCl as a function of distance between collector and generator electrode. Electrodes no. 2, 4, and 8 were used as collector electrodes.

By use of a central electrode of the eight as the generator, there were three possible symmetrically disposed collector electrode pairs that could be used to test the predicted dependence of efficiencies on gap size displayed in Figure 3. Figure 8 shows the results from one such set of experiments and Table III summarizes several such determinations. The experimental results and the simulation are in quite good agreement (Figure 3), at the same θ value with the experimental values consistently slightly lower (ca. 7–10%) than the simulated ones. A possible reason for the discrepancy between the simulation and experiment is that the model does not take into account the effect of intervening nonpotentiostated electrodes. Thus, when using electrode no. 4 as a generator and electrodes no. 2 and 6 as collectors, the presence of electrodes no. 3 and 5 may contribute in some way to the observed collection efficiency. To test this, experiments were carried out to measure collection efficiencies before and after electrochemical removal of the intervening electrodes (see Experimental Section). The collection efficiency in an experiment with generator electrode no. 4 and collector electrodes no. 2 and 6 increased from 49% to 57% after removal of electrodes no. 3 and 5. This suggested that intervening electrodes act to diminish currents.

The dependence of collection efficiency on the distance between the generator and only *one* collector electrode is presented in Table IV and Figures 5 and 9. A collection efficiency of 58% between adjacent electrodes was observed. Upon use of electrode no. 4 as the collector and electrode no. 1 as the generator, the collection efficiency dropped by less than a factor of 2 to 34%. For the no. 1/no. 4 generator–collector pair the electrodes were separated by 8.3 μm between adjacent edges. The generator electrode current amplitude for this pair and all pairs at greater separation was identical with the current amplitude observed with no collector electrode, indicating that there was negligible feedback for the

Table IV. Distance Dependence of Observed Collection Efficiency for a Generator-Single Collector Electrode Pair

generator electrode current, nA		collector electrode current, nA		separation,[a] μm	collection efficiency,[b] %
no. 1	32.0	no. 2	24.0	1.0	58
no. 1	24.0	no. 3	10.0	4.7	42
no. 1	22.0	no. 4	7.5	8.3	34
no. 1	21.5	no. 5	6.0	11.9	28
no. 1	21.0	no. 6	5.0	15.5	24
no. 1	20.5	no. 7	4.5	19.1	22
no. 1	20.5	no. 8	4.0	22.7	20

[a] Separation between nearest edges of a single generator and a single collector electrode (±0.1 μm). [b] The standard deviation in absolute collection efficiency from array to array is ±4%. However, each array shows a smooth decrease in collection efficiency as the collector electrode is farther from the generator electrode.

large separations. For the greatest separation, the no. 1/no. 8 pairing, the collection efficiency was 20%. These results agree well with the symmetrical generator–collector experiments and the simulated results in that the collection efficiency falls off slowly with distance.

The collection efficiency vs. gap size (separation between generator and collector) was further investigated by using two-electrode arrays. The smaller interelectrode spacing of the two-electrode arrays, 0.8 μm, compared to 1.0 μm for the eight-electrode arrays, resulted in a larger collection efficiency for the reduction and reoxidation of $Ru(NH_3)_6^{3+}$: 68% compared to 58%. There are two possible geometric factors at work here that can be considered to affect collection efficiency, i.e., collector electrode area and interelectrode spacing. The improved collection efficiency was caused by the smaller spacing, since results above show that collector area is not a big factor in collection efficiency, Figure 7b vs. Figure 7c. Moreover, the electrodes of the two-wire arrays had smaller areas than did the electrodes of the eight-wire arrays that gave the 58% collection efficiency, Figure 9. It appears that collector area does not have as great an effect on the collection efficiency as the interelectrode spacing, as predicted in part I.

Effect of Increased Platinization of Microelectrodes on the Collection Efficiencies. The strong dependence of collection efficiency on gap size (generator separation from *one* collector) was further investigated by electrochemically depositing relatively large amounts of Pt onto the electrodes to close the gap between adjacent microelectrodes by a significant amount. Two different strategies were employed to minimize the interelectrode spacing. Either large amounts of Pt were deposited on each electrode or one electrode was lightly platinized and the other heavily platinized. Large Pt deposits generally resulted in rough edges along the electrodes. Projections of Pt along the rough edge occasionally led to shorted electrode pairs. The light/heavy deposition strategy preserves one straight edge. Clearly, Pt deposition reduces the gap size, but it also increases the height and width of the electrodes.

Large amounts of Pt were deposited on six of eight electrodes in an array by reduction of $PtCl_4^{2-}$ in 0.1 M K_2HPO_4. Amounts of Pt deposited and resulting dimensions of the electrodes (determined by scanning electron microscopy) are detailed in Table V. Figure 10 displays the large increase in limiting currents and collection efficiency as the gap between adjacent electrodes is decreased to 0.2 μm. At a 1.0 μm separation between lightly platinized electrodes, a collection efficiency of 53% was obtained. For heavily platinized microelectrodes with a spacing of 0.2 μm, a collection efficiency of 83% was observed.

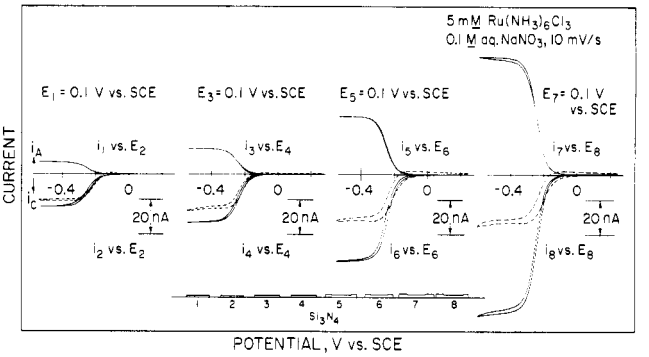

Figure 10. Generation/collection cyclic voltammetry at a series of heavily platinized electrodes in 5 mM $Ru(NH_3)_6Cl_3$ in 0.1 M aqueous $NaNO_3$. Electrode geometries are presented in Table II. Dashed curves represent collectors at open circuit.

Table V. Observed Collection Efficiencies at Heavily Platinized Arrays

electrode	charge passed during $Pt^{2+} \rightarrow Pt^0$, μC	width of electrode, μm	gap size, μm	collection efficiency, %
no. 1	0.0	2.2	1.3	40
no. 2	0.0	2.2		
no. 3	0.25	2.4	1.0	53
no. 4	0.25	2.4		
no. 5	1.25	3.0	0.7	66
no. 6	1.25	2.7		
no. 7	2.00	3.3	0.2	83
no. 8	2.00	3.0		

In another experiment, one electrode was lightly platinized by passing 0.2 μC and the adjacent electrode was heavily platinized by passing 4.0 μC. The heavily platinized electrode was 4.1 μm wide and separated from the lightly platinized electrode by 0.3 μm. The heavily platinized electrodes displayed large nonfaradaic currents and significant cathodic currents for the reduction of H_2O. The lightly platinized electrode situated next to the heavily platinized electrode showed a slight voltammetric cathodic current peak for the reduction of 2 mM $Ru(NH_3)_6^{3+}$. The heavily platinized electrode may impair radial diffusion to the adjacent lightly platinized electrode. A collection efficiency of 80% was obtained when the lightly platinized electrode was connected as the generator electrode and the heavily platinized electrode is connected as the collector electrode. By connection of a lightly platinized electrode as the generator electrode between two heavily platinized collector electrodes, a maximum of 93% collection efficiency was observed. This high collection efficiency was a consequence of the small separation (Figure 3).

The gap between two-electrode arrays was similarly narrowed. For example, one electrode can be plated with 0.2 μC of Pt from $PtCl_4^{2-}$ in solution, and the other electrode can be plated with 1.75–2.0 μC of Pt. The resulting widths were 1.5 μm and 2.2 μm, respectively, separated by 0.3–0.4 μm, which was very similar to that in the analogous electrodes of an eight-electrode array. An 80% collection efficiency for the reoxidation of $Ru(NH_3)_6^{2+}$ was observed, identical with that observed at the eight-electrode array. This experiment confirmed the suggestion that interelectrode spacing is the dominant factor controlling collection efficiencies, and not collector widths, since the widths in the two-electrode arrays are different than those in the eight-electrode arrays.

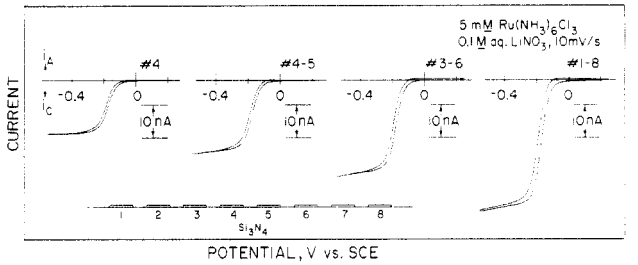

Figure 11. Slow scan rate cyclic voltammetry in 5 mM $Ru(NH_3)_6Cl_3$ in 0.1 M aqueous $LiNO_3$ at one, two adjacent, four adjacent, and eight adjacent electrodes.

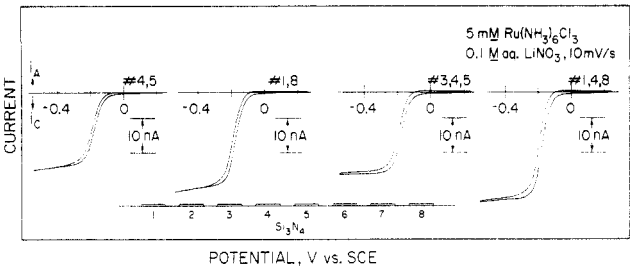

Figure 12. Slow scan rate cyclic voltammetry in 5 mM $Ru(NH_3)_6Cl_3$ in 0.1 M aqueous $LiNO_3$ at adjacent vs. interspaced electrodes.

Shielding Effects at Microelectrode Arrays. To demonstrate shielding in the sense developed in part I, various combinations of the eight electrodes were driven together as the working electrode in a conventional three-electrode linear potential sweep voltammetry configuration for the reduction of 5 mM $Ru(NH_3)_6Cl_3$ in 0.1 M $LiNO_3$. The basic finding was that quasi-steady-state cathodic current amplitudes were not directly proportional to the combined areas of the closely spaced electrodes. Figure 11 presents the results of linear potential sweep voltammetry at one, two adjacent, four adjacent, and all eight electrodes. Two adjacent electrodes displayed 61% of the limiting cathodic current expected by simply doubling the current observed at a single electrode. Driving more adjacent electrodes incrementally decreased the percentage of observed current relative to that expected by simply multiplying the current at a single electrode by the number of electrodes driven together. Driving all eight electrodes together resulted in a limiting cathodic current that was only 28% of 8 times the limiting current at a single electrode. Figure 12 demonstrates the effects of driving a group of electrodes spread out across the array in contrast to driving the same number of adjacent electrodes. The current at two adjacent electrodes was 61% of 2 times the current at a single microelectrode ($S_F = 0.39$). A total of 89% of 2 times the current at a single electrode was observed ($S_F = 0.11$) by driving electrodes no. 1 and no. 8, separated by 23 μm between nearest edges across the microelectrode array. At three adjacent electrodes, 46% of 3 times the current at a single electrode was observed in good agreement with the simulated result at $\log \theta = 4.3$ of $S_F = 0.56$. With a spread of the three electrodes across the array, the limiting cathodic current observed increased to 64% of 3 times the current at a single electrode. The importance of radial diffusion of redox species to the electrodes is clear. The effective radial diffusion to the combined electrode area was reduced by driving the closely spaced electrodes together.

Collection Efficiency of the Intermediate in an EC′ Reaction. So far we have described experiments investigating the generation and collection of a stable redox reagent $Ru(NH_3)_6^{2+}$. Now we describe preliminary results for an intermediate that is unstable in the presence of dissolved O_2 and follows the EC′ mechanism in eq 1 and 2. The type of reaction that we have chosen for study is the reduction ($2e^-/2H^+$) of

Table VI. Grid Parameters for the Digital Simulation

		J direction (perpendicular to the electrodes)			
		N direction (parallel to the electrodes)			
limits[a]	element width	inner boundary	outer boundary	concentration
all *J*	$\Delta y(J) = \Delta y \exp[\beta(J-1)]$	$y'(J) = \Delta y \dfrac{\exp[\beta(J-1)]-1}{\exp[\beta]-1}$	$y''(J) = \Delta y \dfrac{\exp[\beta J]-1}{\exp[\beta]-1}$	$\bar{y}(J) = \Delta y \dfrac{\exp[\beta(J-1/2)]-1}{\exp[\beta]-1}$
$N1 \le N \le N4^b$	$\Delta x(N) = \Delta x$	$x'(N) = (N-1)\Delta x$	$x''(N) = N\Delta x$	$\bar{x}(N) = (N-1/2)\Delta x$
$N > N4^{b,c}$	$\Delta x(N) = \Delta x \exp[\beta(N-N4-1)]$	$x'(N) = \Delta x \dfrac{\exp[\beta(N-N4-1)]-1}{\exp[\beta]-1}$	$x''(N) = \Delta x \dfrac{\exp[\beta(N-N4)]-1}{\exp[\beta]-1}$	$\bar{x}(N) = \Delta x \dfrac{\exp[\beta(N-N4-1/2)]-1}{\exp[\beta]-1}$

[a] $\Delta x = \Delta y$ in all cases. [b] $N4$ is the last uniform element corresponding to the electrode edge. [c] For the grid in Figure 1B, these equations were further modified to account for the expanding grid to the left of the generator electrode, $N < N1$, where $N1$ is the first uniform element of the electrode surface.

Table VII. Summary of Simulation Diffusion Constants

limits[a]	inner boundary	outer boundary
$J \geq 2$	$D'(J) = \dfrac{D_M}{\exp[2\beta(J - 5/4)]}$	$D''(J) = \dfrac{D_M}{\exp[2\beta(J - 3/4)]}$
$J = 1$	$D'(1) = D_M \dfrac{\exp[\beta] - 1}{\exp[\beta/2] - 1}$	$D''(1) = \dfrac{D_M}{\exp[2\beta(J - 3/4)]}$
$N < N4$[b,c]	D_M	D_M
$N > N4 + 1$[b,c]	$D'(N) = \dfrac{D_M}{\exp[2\beta(N - N4 - 5/4)]}$	$D''(N) = \dfrac{D_M}{\exp[2\beta(N - N4 - 3/4)]}$
$N = N4 + 1$[b,c]	D_M	$D''(N) = \dfrac{D_M}{\exp[2\beta(N - N4 - 3/4)]}$

[a] In all cases $\Delta x = \Delta y$. [b] $N4$ corresponds to the last element of the electrode surface. [c] For the grid in Figure 1B, the equations were modified to account for the grid expanding to the left of electrode A, i.e., for $N < N1$.

the water-soluble benzoquinone (Q) to QH_2, which undergoes a rapid follow-up reaction with dissolved O_2, eq 9 and 10.

$$Q + 2e^- + 2H^+ \rightleftarrows QH_2 \quad (9)$$

$$QH_2 + O_2 \rightarrow Q + H_2O_2 \quad (10)$$

Q = 2,5-dichloro-3,5-bis[[2-(dimethylpropylamino)-ethyl]amino]benzoquinone

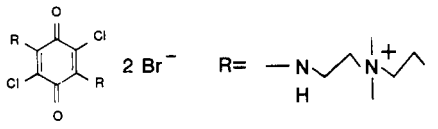

The rate constant, k, was estimated from rotating disk data for immobilized quinone, Q, on a W electrode to be $\geq 0.65 \times 10^5$ M^{-1} s^{-1} (*20*). We now describe experiments aimed at a direct measurement of this rate constant from the electrochemistry of Q at an ultramicroelectrode array. Figure 13a shows the generation and collection of QH_2 at adjacent electrodes after the aqueous Q solution (5 mM, pH 7.2 Tris buffered) was thoroughly deoxygenated by purging with N_2. The generator electrode was swept from 0.0 to −0.8 V to reduce Q (E° = −0.34 V vs. SCE) (*21*) and the collector was held at 0.0 V, a potential sufficiently positive to redoxidize the generated QH_2. The collection efficiency of 57% was close to that observed at the same two electrodes with Ru^{3+} (58%). This indicated that no follow-up reaction of QH_2 occurred in the absence of O_2. For a single electrode with the collector turned off (not shown), the observed generator current was used to estimate a diffusion coefficient based on the observed currents for Ru^{3+} reduction (diffusion coefficient for Ru^{3+} taken as 0.71×10^{-5} cm^2 s^{-1} (*30*)) and assuming that the reaction remained a simple $2e^-/2H^+$ reduction at Au, as it was at W electrodes (*21*, *22*). We know that the current is proportional to the number of electrons and the diffusion coefficients from eq 8. Thus, we calculated a diffusion coefficient, $D_Q = 0.35 \times 10^{-5}$ cm^2 s^{-1}, for Q.

Figure 13 also shows the changes that occur when the same solution was purged with air (Figure 13b) and pure O_2 (Figure 13c). We observed the following: (1) the generator current was increased as expected for the catalytic regeneration of Q (eq 10); (2) the magnitude of the collection current was decreased, indicating the consumption of the intermediate QH_2 as it diffuses to the collector electrode. The increase in the generator current (obtained by subtracting the diffusion limited current in the absence of O_2 from the total current) can be used to calculate a value for the rate constant for the reaction of QH_2 with O_2 by substituting in the following expression for the catalytic current, i_{cat}, eq 11. This equation

$$i_{cat} = nFAD_QC_Q(kC_{O_2}/D_{O_2})^{1/2} \quad (11)$$

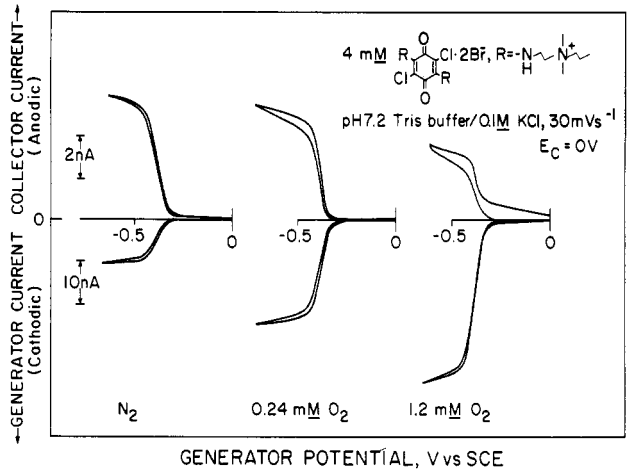

Figure 13. Generation/collection curves at Au microelectrodes for the reduction of 5 mM quinone (Q) in pH 7.2 buffered (Tris/KCl) aqueous solution with (left to right) N_2, air, and O_2 purge.

was derived in a similar fashion to that given in ref 18 for pseudo-first-order reaction of Q. Taking the concentration of O_2 in air-saturated aqueous solution as 0.24 mM (*31*), using the value of D_Q calculated earlier and taking D_{O_2} (*30*) to be 2.6×10^{-5} cm^2 s^{-1}, we obtained a rate constant of 7 (±5) $\times 10^6$ M^{-1} s^{-1}, which was an average value taken from several experiments at different Q and O_2 concentrations. (The error stems from the error in measuring the current and the approximation involved in calculating the area of the entire surface of the electrode, including contributions from the walls of the electrode.) This value compares with the lower limit of 0.65×10^5 M^{-1} s^{-1} calculated previously for similar surfaced-confined quinones. As a check that the pseudo-first-order conditions necessary to apply eq 8, i.e., diffusive flux of O_2 >> flux required to sustain reaction with QH_2 are operating, one can derive eq 12 (*18*). This condition was amply

$$(D_{O_2}C_{O_2}/W)[5.553/(\ln \theta) - 6.791/(\ln \theta)^2] >> D_QC_Q(kC_{O_2}/D_{O_2})^{1/2} \quad (12)$$

satisfied in the case of purging the solution with pure O_2. There was direct evidence for an excess of O_2, since a "tail" was seen at the most negative part of the sweep for the direct reduction of O_2 at the Au surface.

Turning our attention once again to the collection currents shown in Figure 13 we see that the current for QH_2 reoxidation was approximately halved in the presence of 1.2 mM O_2. While a quantitative description of this must await a full digital simulation, the decrease in collection current may be qualitatively explained on the basis of transit time arguments

similar to those used in the rotating ring–disk experiment (*32*). From a random walk model the distance, x, traveled by the diffusing quinone in time t is $x^2 \approx (2D_Q t)$. Hence, the transit time to cross the 1.2 μm interelectrode spacing was 1 ms, which was the same order as the half-life of the quinone in the pseudo-first-order reaction with 1.2 mM O_2 ($t_{1/2}(kC_{O_2}) = 2$ ms).

In the recent literature on the electrocatalytic reduction of O_2 by both soluble (*33*, *34*) and insoluble (*31*) catalysts, there has been disagreement concerning the relative importance of the contributions from heterogeneous reactions of supposed soluble catalysts. Shigehara and Anson (*31*) have pointed out that the ratio of the catalytic currents from the adsorbed and dissolved catalysts is given by eq 13, where Γ_{cat} is the surface

$$i_{ads}/i_{sol} = k^{1/2}\Gamma_{cat}/(D_{O_2}{}^{1/2}C_{cat}{}^{1/2}) \quad (13)$$

excess of the adsorbed catalyst. Even with submonolayer coverage (barely detectable by rotating disk techniques), say 10^{-11} mol cm^{-2}, and a rate constant of $k = 4 \times 10^{10}$ M^{-1} s^{-1}, the adsorbed catalyst would have a comparable turnover rate to the dissolved catalyst present in millimolar concentration. In the context of the quinone experiment described in this paper, the absence of such complications was ensured by cleaning the electrodes prior to each measurement. Furthermore, the collection currents for the dissolved QH_2 species were decreased in accordance with the half-life calculated assuming a solution reaction with O_2.

CONCLUSIONS

Steady-state currents are observed for linear potential sweep voltammetry of solution redox species at microelectrodes. The significant contribution of radial diffusion of redox species to and from the microelectrode obviates the need for forced hydrodynamics otherwise necessary to obtain steady current behavior. Moreover, the collection efficiencies attainable at microelectrode arrays are significantly larger than those usually obtained at RRDEs. The observation that the limiting current for the redox reaction of a solution species at two closely spaced microelectrodes is significantly less than the sum of the currents observed at each microelectrode separately provides evidence for shielding and the importance of radial diffusion.

From the digital simulation of microelectrode arrays and the use of these arrays as RRDE-type probes, we can draw several conclusions. One of the key factors allowing these systems to work is the small gap size. As the interelectrode spacing is reduced by Pt deposition, larger collection efficiencies are obtained in generation–collection experiments. In this paper, we report efficiencies of ca. 80% for gap sizes of ca. 0.2 μm. Although it may be possible to reduce the gap further, the gain in efficiency will probably not be sufficient to justify the efforts. In addition, with smaller and smaller gaps, migration may become important. The effect of migration may be useful for the study of intermediates.

The digital simulations reported here are useful for simulating current–time behavior for single microband electrodes as well as for predicting the collection efficiency of RRDE-type experiments at arrays. In future work, we hope to simulate in detail the experiments of homogeneous follow-up reactions briefly outlined in this paper.

ACKNOWLEDGMENT

We thank Diane K. Smith for the sample of the quinone compound and S. W. Feldberg for his assistance and comments on the digital simulations.

APPENDIX: DIGITAL SIMULATION MODEL

The digital simulation methods follow those used previously in electrochemical problems combining the uniform (*24*, *25*) and exponentially expanding space grids (*26*, *28*), Figure 1. The distance in the N direction across the electrode surface, NELE, and the interelectrode gap, NGAP, is divided by a uniform space grid while in the J direction, perpendicular to the substrate and beyond the outer electrode edge in the parallel, N direction, the grid expands exponentially. Each part of the problem will be treated separately beginning with the expanding portions of the simulation. The mathematical treatment generally applies to simulations of a single band and to arrays of band electrodes.

The development of the equations describing the expanding grid elements follows that in ref 26. The width of the expanding box, $\Delta y(J)$ is given by eq A1, which reduces to the uniform grid size when $\beta = 0$. β is the exponential grid factor

$$\Delta y(J) = \Delta y \exp[\beta(J - 1)] \quad (A1)$$

and $\beta = 0.5$ (*26*) for all expanding portions of the grid. The outer boundary of the box is at $y''(J)$, eq A2, while the inner boundary is at $y'(J)$, eq A3. The concentration within each

$$y''(J) = \Delta y(\exp[\beta J] - 1)/(\exp[\beta] - 1) \quad (A2)$$

$$y'(J) = \Delta y(\exp[\beta(J - 1)] - 1)/(\exp[\beta] - 1) \quad (A3)$$

expanded volume element is taken at the position given in eq A4. In the limit as $\beta \to 0$, eq A2–A4 reduce to

$$\bar{y}(J) = \Delta y(\exp[\beta(J - 1/2)] - 1)/(\exp[\beta] - 1) \quad (A4)$$

those for a uniform grid where the concentration is taken at the midpoint of each box. A summary of the grid parameters is presented in Table VI.

The finite difference form of Fick's second law, eq A5, in

$$\partial C/\partial t = D[(\partial^2 C/\partial x^2) + (\partial^2 C/\partial y^2)] \quad (A5)$$

two dimensions is given by eq A6 and can be used to calculated

$$[C(x,y,t+\Delta t) - C(x,y,t)]/\Delta t = D[(C(x+\Delta x,y,t) - C(x,y,t))/\Delta\bar{x}^2 - (C(x,y,t) - C(x-\Delta x,y,t))/\Delta\bar{x}^2 + (C(x,y+\Delta y,t) - C(x,y,t))/\Delta\bar{y}^2 - (C(x,y,t) - C(x,y-\Delta y,t))/\Delta\bar{y}^2] \quad (A6)$$

the change in concentration due to diffusion in a *uniform space grid* where $\Delta x = \Delta y$ for all N and J. The diffusion coefficient, D, the time increment, Δt, and the space increment, Δx, can be gathered into dimensionless simulation diffusion constant, D_m, eq A7. For our simulations, we assume

$$D_m = D\Delta t/\Delta x^2 = D\Delta t/\Delta y^2 \leq 0.25 \quad (A7)$$

that $D_{Ox} = D_{Red}$ and a value of $D_m = 0.24$ is used throughout.

The flux, f, in each of the volume elements is calculated by substituting the values of $\Delta x(N)$, $\Delta y(J)$, $\bar{x}(N)$, and $\bar{y}(J)$ from Table VI into eq A6 which results in eq A8. The flux

$$f = D\Delta t/\Delta y(J)[[C(N,J+1) - C(N,J)]/[\bar{y}(J+1) - \bar{y}(J)] - [C(N,J) - C(N,J-1)]/[\bar{y}(J) - \bar{y}(J-1)]] + D\Delta t/\Delta x(N)[[C(N+1,J) - C(N,J)]/[\bar{x}(N+1) - \bar{x}(N)] - [C(N,J) - C(N-1,J)]/[\bar{x}(N) - \bar{x}(N-1)]], \text{ for } N,J \geq 2 \quad (A8)$$

equation, eq A8 can be simplified by redefining the dimensionless diffusion constant taking into account the modified boundaries so that now the simulation diffusion coefficients are a function of distance. At the outer boundary, $y''(J)$, of the expanded elements, $D''(J)$ is given by eq A9, while eq A10

$$D''(J) = D_M/\exp[2\beta(J - 3/4)] \quad (A9)$$

$$D'(J) = D_M/\exp[2\beta(J - 5/4)], J \geq 2 \quad (A10)$$

is the expression for the diffusion constant at the inner boundary. A summary of the diffusion constants is presented in Table VII.

To calculate the current, the flux at the electrode surface must be calculated. The electrode width, W, is divided by

the number of boxes corresponding to the electrode, NELE, such that eq A11 holds. During a simulation time iteration,

$$\Delta x = \Delta y = W/\mathrm{NELE} \quad \text{(A11)}$$

K, the flux in each of the NELE boxes representing the electrode is calculated and the individual fluxes, $f_K(N)$, are then summed to yield the total flux, f_K. The average flux in the box N at the electrode is given by eq A12. Since eq A12

$$f_K(N) = D'(1)(C(N,1) - C(N,0)) \quad \text{(A12)}$$

is the average flux during the time increment, K, the flux at $t = K\Delta t$ is given by the average of the fluxes, $f_K(N) + f_{K+1}(N)$ and the total dimensionless flux, F_K, is calculated by eq A13.

$$F_K = \sum_{N=1}^{\mathrm{NELE}} (f_K(N) + f_{K+1}(N))/(2D_m) \quad \text{(A13)}$$

The total flux, F_K, is related to the corresponding dimensionless current, $Z(K)$, by eq A14. $Z(K)$ can be expressed for

$$F_K/\mathrm{NELE} = i/nFDCl = Z(K) \quad \text{(A14)}$$

various time domains which depend on the dimensionless parameter θ defined in eq A15. In eq A15 D is the real

$$\theta = 4Dt/W^2 = 4D_mK/(\mathrm{NELE})^2 \quad \text{(A15)}$$

diffusion coefficient (cm^2/s), t is the real time in (s), W is the electrode width (cm), while D_m, K, and NELE are the corresponding dimensionless simulation parameters. As shown by Tallman et al. (*29*), in the limit of long times, $\log \theta >$ ca. 2.5, the total dimensionless flux is given by eq. A16. For short

$$Z(K) = i/nFDCl = 5.553/(\ln \theta) - 6.791/(\ln \theta)^2 \quad \text{(A16)}$$

times, i.e., $\log \theta <$ ca. 1.0, the flux can be calculated by eq A17 (see Figure 2) (*29*, *35*) where eq A16 derives from the long time

$$Z(K) = i/nFDCl = 2/(\pi\theta)^{1/2} + 1 \quad \text{(A17)}$$

expression for the current at a band electrode (*29*) and eq. A17 follows from eq 40 in ref 35.

Registry No. Q, 103190-68-7; QH_2, 103190-69-8; $Ru(NH_3)_6^{3+}$, 18943-33-4; $Ru(NH_3)_6^{2+}$, 19052-44-9; $Ru(NH_3)_6Cl_3$, 14282-91-8; LiCl, 7447-41-8; $LiNO_3$, 7790-69-4; $NaNO_3$, 7631-99-4; KCl, 7447-40-7; O_2, 7782-44-7; Au, 7440-57-5; Pt, 7440-06-4.

LITERATURE CITED

(1) Wightman, R. M. *Anal. Chem.* **1981**, *53*, 1125A, and references therein.
(2) Bond, A. M.; Fleischmann, M.; Robinson, J. *J. Electroanal. Chem.* **1984**, *168*, 299.
(3) Bond, A. M.; Fleischmann, M.; Robinson, J. *J. Electroanal. Chem.* **1984**, *172*, 11.
(4) Bindra, P.; Brown, A. P. Fleischmann, M.; Pletcher, D. *J. Electroanal. Chem.* **1975**, *58*, 31.
(5) Mallouk, T. E.; Cammarata, V. C.; Crayston, J. A.; Wrighton, M. S., submitted for publication in *J. Phys. Chem.*
(6) White, H. S.; Kittlesen, G. P.; Wrighton, M. S. *J. Am. Chem. Soc.* **1984**, *106*, 5375.
(7) Kittlesen, G. P.; White, H. S.; Wrighton, M. S. *J. Am. Chem. Soc.* **1984**, *106*, 7389.
(8) Paul, E. W.; Ricco, A. J.; Wrighton, M. S. *J. Phys. Chem.* **1985**, *89*, 1441.
(9) Thormann, W.; van den Bech, P.; Bond, A. M. *Anal. Chem.* **1985**, *57*, 2764.
(10) Chidsey, C. E.; Feldman, B. J.; Lundgren, C.; Murray, R. W. *Anal. Chem.* **1986**, *58*, 601.
(11) Kittlesen, G. P.; White, H. S.; Wrighton, M. S. *J. Am. Chem. Soc.* **1985**, *107*, 7373.
(12) Kittlesen, G. P.; Wrighton, M. S. *J. Mol. Electron.*, in press.
(13) Thackeray, J. W.; White, H. S.; Wrighton, M. S. *J. Phys. Chem.* **1985**, *89*, 5133.
(14) Wrighton, M. S. *Comments Inorg. Chem.*, in press.
(15) Albery, W. J.; Hitchman, M. L. In *Ring-Disk Electrodes*; Clarendon Press: Oxford, 1971.
(16) Bruckenstein, S.; Miller, B. *Acc. Chem. Res.* **1977**, *10*, 54.
(17) Bard, A. J.; Faulkner, L. R. In *Electrochemical Methods*; Wiley: New York, 1980; p 429.
(18) Fleischmann, M.; Lassere, F.; Robinson, J.; Swan, D. *J. Electroanal. Chem.* **1984**, *177*, 97.
(19) Dayton, M. A.; Ewing, A. G.; Wightman, R. M. *Anal. Chem.* **1980**, *52*, 2392.
(20) Miller, B.; Visco, R. E. *J. Electrochem. Soc.* **1968**, *115*, 251.
(21) Smith, D. K.; Calabrese, G. S.; Wrighton, M. S., unpublished results.
(22) Calabrese, G. S.; Buchanan, R. M.; Wrighton, M. S. *J. Am. Chem. Soc.* **1982**, *104*, 5786.
(23) Calabrese, G. S.; Buchanan, R. M.; Wrighton, M. S. *J. Am. Chem. Soc.* **1983**, *105*, 5594.
(24) Feldberg, W. S. In *Electroanalytical Chemistry*; Bard, A. J., Ed.; Marcel Dekker: New York, 1979; Vol. 3.
(25) Maloy, J. T. In *Laboratory Techniques in Electroanalytical Chemistry*; Kissinger, P. T., Ed., Marcel Dekker: New York, 1984.
(26) Feldberg, W. S. *J. Electroanal. Chem.* **1981**, *127*, 1.
(27) Reller, H.; Kirowa-Eisner, E.; Gileadi, E. *J. Electroanal. Chem.* **1984**, *161*, 247.
(28) Joslin, T.; Pletcher, D. *J. Electroanal. Chem.* **1974**, *49*, 171.
(29) Coen, S.; Cope, D. K.; Tallman, D. E., submitted for publication in *J. Electroanal. Chem.*
(30) Kovach, P. M.; Caudill, W. L.; Peters, D. G.; Wightman, R. M. *J. Electroanal. Chem.* **1982**, *185*, 285.
(31) Shigehara, K.; Anson, F. C. *J. Phys. Chem.* **1982**, *86*, 2776.
(32) Bruckenstein, S. B.; Feldman, G. A. *J. Electroanal. Chem.* **1965**, *9*, 395.
(33) Kobayashi, N.; Fujihara, M.; Osa, T.; Kuwana, T. *Bull. Chem. Soc. Jpn.* **1980**, *53*, 2195.
(34) Forshey, P. A.; Kuwana, T. *Inorg. Chem.* **1983**, *22*, 699.
(35) Oldham, K. B. *J. Electroanal. Chem.* **1981**, *122*, 1.

RECEIVED for review January 24, 1986. Accepted May 5, 1986. We thank the following agencies for support of this research: National Science Foundation (CHE 8402135), the Office of Naval Research, and the Defense Advanced Research Projects Agencies.

CORRESPONDENCE

Charge Exchange in Binary Mixtures of Polycyclic Aromatic Hydrocarbons Using Photoionization–Ion Mobility Spectrometry

Sir: Ion mobility spectrometry (IMS) has been limited in convenience of operation and breadth of application by complications in processes used to create product ions from gaseous analyte. While chemical ionization (CI) may provide sensitivities directly in the low-parts-per-billion or sub-parts-per-billion ranges without sample enrichment (*1–3*), analytical response with mixtures is governed by competitive ionization reactions (*4–6*). Consequently, analysts typically have limited or no external control (apart from choice of reagent gas) over IMS selectivity or interferences. Indeed, some early reports on poor resolution of binary mixtures in IMS (*7*) may have been due to preferential ionization rather than fundamental limitations in separations based on ion mobility. Although competitive ionization reactions were recognized by some workers early in IMS development (*8*, *9*), selectivity in competitive CI reactions, including proton af-

0003-2700/86/0358-2331$01.50/0